3290 *Chem. Mater.* **2009,** *21,* 3290–3296
DOI:10.1021/cm900820p

CHEMISTRY OF MATERIALS
Article

Intermediate-Temperature Ceramic Fuel Cells with Thin Film Yttrium-Doped Barium Zirconate Electrolytes

Joon Hyung Shim,*[,†] Joong Sun Park,[†] Jihwan An,[†] Turgut M. Gür,[‡] Sangkyun Kang,[§] and Fritz B. Prinz[†,‡]

[†]*Department of Mechanical Engineering, Stanford University, Stanford, California 94305,* [‡]*Department of Material Science and Engineering, Stanford University, Stanford, California 94305, and* [§]*Samsung Advanced Institute of Technology, Samsung Electronics, Giheung, Gyeonggi-do, Korea*

Received March 24, 2009. Revised Manuscript Received May 25, 2009

Structural and microstructural properties as well as the fuel cell performance of anhydrous proton conducting yttria-doped barium zirconate (BYZ) membranes were investigated. The membranes were nominally about 100 nm thick and were fabricated by both atomic layer deposition (ALD) and pulsed laser deposition (PLD) techniques on micromachined Si substrates. Electrochemical cells (H_2, Pt/BYZ/Pt, air) were fabricated using porous platinum electrodes deposited by sputtering. The cells were tested in the temperature regime 200−450 °C. Power densities of 136 mW/cm^2 at 400 °C employing a BYZ membrane fabricated by ALD and 120 mW/cm^2 at 450 °C employing a BYZ fabricated by PLD clearly represent the highest reported values in the literature at these temperatures. The difference in the cell performances for the ALD BYZ versus PLD BYZ membranes is attributed to differences in their surface morphology and interfacial microstructure.

Introduction

Acceptor-doped perovskites of the general formula ABO_3 (A;Ba, B:Ce, Zr) have attracted attention as potential electrolyte material for next generation protonic devices including fuel cells, membrane reactors, separators, and gas reformers because of their high ionic conductivity.[1−9] In this family of perovskites, protons conduct through hydroxide defects that are produced by incorporation of water molecules into oxide ion vacancies in the crystal lattice. This protonation process can be expressed in Kröger-Vink notation as

$$H_2O + V_O^{\bullet\bullet} + O_O^x \Leftrightarrow 2OH_O^{\bullet} \quad (1)$$

The relative instability of some of these materials in acidic environments, however, has limited their practical use. It has been reported that doped $BaCeO_3$ perovskites decompose into barium carbonate and ceria upon exposure to carbon dioxide at elevated temperatures and that this phenomenon is particularly severe in yttria-doped barium cerate, which exhibits high proton conductivity.[10−12] In the presence of water, it was reported that $BaCeO_3$ easily decomposed into $Ba(OH)_2$, causing barium deficiency and decreased ionic conductivity.[4] In comparison, alkaline-earth-metal zirconates such as $SrZrO_3$ and $BaZrO_3$ are known to be chemically more stable, especially against acidic gases such as CO_2.[13] Moreover, doped $BaZrO_3$ has higher proton conductivity compared to doped $BaCeO_3$ in the intermediate temperature range 200−500 °C.[4]

Thin film doped perovskites, including doped $BaCeO_3$ and doped $BaZrO_3$, have been tested as electrolytes for protonic ceramic fuel cells (PCFC) at intermediate temperatures around 500−700 °C.[4,14−16] The best-performing cell demonstrated 900 mW/cm^2 at 500 °C with yttrium-doped $BaZr_{0.5}Ce_{0.5}O_3$.[14] Those electrolytes have been synthesized in the range of several micrometers in thickness. Previously, our group had reported the performance of oxide ion conducting fuel cells employing nanoscale yttria-stabilized zirconia (YSZ) electrolytes.[17−19]

*To whom correspondence should be addressed. E-mail: shimm@stanford.edu.

(1) Iwahara, H.; Uchida, H.; Ono, K.; Ogaki, K. *J. Electrochem. Soc.* **1988**, *135*, 529–533.
(2) Slade, R. C. T.; Singh, N. *Solid State Ionics* **1991**, *46*, 111–115.
(3) Munch, W.; Seifert, G.; Kreuer, K. D.; Maier, J. *Solid State Ionics* **1997**, *97*, 39–44.
(4) Kreuer, K. D. *Annu. Rev. Mater. Res.* **2003**, *33*, 333–359.
(5) Kuwata, N.; Sata, N.; Tsurui, T.; Yugami, H. *Jpn. J. Appl. Phys., Part 1* **2005**, *44*, 8613–8618.
(6) Iwahara, H.; Uchida, H.; Morimoto, K. *J. Electrochem. Soc.* **1990**, *137*, 462–465.
(7) Bonanos, N.; Ellis, B.; Mahmood, M. N. *Solid State Ionics* **1991**, *44*, 305–311.
(8) Hibino, T.; Hashimoto, A.; Suzuki, M.; Sano, M. *J. Electrochem. Soc.* **2002**, *149*, A1503–A1508.
(9) Coors, W. G. *J. Electrochem. Soc.* **2004**, *151*, A994–A997.
(10) Shima, D.; Haile, S. M. *Solid State Ionics* **1997**, *97*, 443–455.
(11) Wu, Z. L.; Liu, M. L. *J. Electrochem. Soc.* **1997**, *144*, 2170–2175.
(12) Ma, G. L.; Shimura, T.; Iwahara, H. *Solid State Ionics* **1998**, *110*, 103–110.
(13) Iwahara, H.; Yajima, T.; Hibino, T.; Ozaki, K.; Suzuki, H. *Solid State Ionics* **1993**, *61*, 1–3.
(14) Iijima, M; Ito, N; Matsumoto, S.; Iguchi, S *Mater. Res. Soc. Symp. Proc.* **2007**, *972*, 0972-AA01-08.
(15) Balachandran, U.; Lee, T. H.; Ma, B.; Dorris, S. E. *Mater. Res. Soc. Symp. Proc.* **2007**, *972*, 0972-AA01-09.
(16) Ito, N.; Iijima, M.; Kimura, K.; Iguchi, S. *J. Power Source* **2005**, *152*, 200.
(17) Huang, H.; Nakamura, M.; Su, P.; Fasching, R.; Saito, Y.; Prinz, F. B. *J. Electrochem. Soc.* **2007**, *154*, b20–b24.
(18) Shim, J. H.; Chao, C.; Huang, H.; Prinz, F. B. *Chem. Mater.* **2007**, *19*, 3850–3854.
(19) Su, P.; Chao, C.; Shim, J. H.; Fasching, R.; Prinz, F. B. *Nano Lett.* **2008**, *8*, 2289–2292.

Published on Web 06/17/2009

To our knowledge, however, there has been no published report about proton-conducting ultrathin film fuel cells employing nanoscale doped-perovskite electrolyte membranes.

In this work, we have fabricated and characterized ultrathin yttrium-doped $BaZrO_3$ (BYZ) membranes as ceramic electrolytes for protonic ceramic fuel cells (PCFC) using pulsed laser deposition (PLD) and atomic layer deposition (ALD) techniques. The electrolyte is fabricated as a freestanding membrane with a thickness of ~100 nm. The current−voltage ($I-V$) characteristics of these cells using nanoscale BYZ electrolytes were measured in the temperature range 200−450 °C.

Experimental Section

Ultrathin BYZ films were fabricated using ALD by sequential deposition of its component oxides (BYZ = BaO + ZrO_2 + Y_2O_3). For this purpose, bis(propyltetramethylcyclopentadienyl)barium ($Ba(PrMe_4Cp)_2$) (Alfa Aesar), tetrakis(dimethylamido)zirconium ($Zr(NMe_2)_4$) (Sigma Aldrich), and tris(methylcyclopentadienyl)yttrium ($Y(MeCp)_3$) (Strem Chemical) were used as precursors for BaO, ZrO_2, and Y_2O_3 deposition, respectively. Distilled water was used as the oxidant for each deposition cycle.

A wide range of precursors, including halides,[20−22] alkoxides,[23,24] β-diketonates,[25] organometallics[26] and alkyl amides,[27] have been studied for ALD of ZrO_2. Metal amides have attracted particular attention because of their superior thermal resistivity against ligand decomposition and excellent reactivity with water toward oxide formation at relatively low temperatures below 250 °C.[27] Several studies have reported successful ALD of Y_2O_3 using $Y(thd)_3$ (thd = 2,2,6,6-tetramethyl-3,5-heptanedionate),[28] $Y(^iPr_2amd)_3$ ($^iPr_2amd$ = diisopropylacetamidinate),[29] $Y(Cp)_3$, and $Y(MeCp)_3$.[30] Among those precursors, the Cp-type precursor demonstrated good reactivity with water to form Y_2O_3.[30] In contrast, there are only a select few precursors for ALD of barium that exhibit sufficient vapor pressure and thermal stability. Only cyclopentadienyl-type precursors were successfully used for ALD of oxides with water.[31]

A customized reactor equipped with automated temperature, pressure, and flow controls was designed and built to process 4 in. diameter silicon wafers that were employed as micromachined substrates for this work. Precursors and oxidants were stored in quartz cylinders and heated for source evaporation. Argon gas (10 sccm) was used as the transport gas for delivering the precursor vapors into the reaction chamber. Deposition was carried out at a pressure of 0.1 Torr. Water vapor and zirconium precursor gas were pulsed into the chamber using solenoid valves. A Fujikin diaphragm valve, specially designed for high-temperature operation up to 350 °C of source heating, was used for controlled delivery of the barium and yttrium precursors. The barium, zirconium, and yttrium precursors were heated to 230, 75, and 190 °C, respectively, for source evaporation, while water was kept at room temperature. A 500 μm thick Si(100) wafer with 200 nm thick Si_3N_4 overcoat on both sides was used as the substrate for this experiment.

For PLD fabrication of BYZ membranes, a sintered $BaZr_{0.8}Y_{0.2}O_{3-\delta}$ pellet (Praxair Inc.) was used as the target material. A Lambda Physik 248 nm KrF excimer laser with an energy density of 3.0 J/cm^2 per pulse was used to ablate the target. The substrate temperature was varied from 400−800 °C during deposition, and the pressure of background oxygen was 100 mTorr. After deposition, samples were cooled under an oxygen pressure of 300 Torr for over 30 min. The deposition rate was about 0.3 Å/pulse. The distance between the target and the substrate was set as 65 mm. A 500 μm thick Si(100) wafer with a 200 nm Si_3N_4 coating on both sides was used as a substrate for this experiment also.

ALD BYZ films were characterized both as-deposited and after annealing at 600−800 °C in 250 Torr of pure oxygen. PLD BYZ films were characterized in relationship to their deposition temperature of 400−800 °C. Film composition was analyzed by X-ray photoelectron spectroscopy (XPS) in a SSI S-Probe monochromated XPS spectrometer with Al Kα radiation (1486 eV). The crystallinity and structural phase of the deposited films were analyzed by X-ray diffraction (XRD) techniques using a PANalytical X'Pert PRO XRD system (Cu Kα X-ray with λ = 1.54 Å), and the symmetrical $\theta/2\theta$ scan method was employed for phase analysis. The performance of nano-BYZ membranes as fuel cell electrolytes was measured in the $I-V$ domain at temperatures from 200 to 450 °C. For the $I-V$ data collection, a Gamry FAS2 Femtostat system was used. The anode side of the fuel cell sample was sealed onto a small chamber in which pure dry hydrogen was circulated as fuel. The cathode side was exposed to ambient air as the oxygen source.

For fuel cell fabrication, typical Si-based microelectromechanical (MEMS) processing methods were used for the substrate. The Si_3N_4-coating layer on one side was patterned to fabricate open window structures in the Si substrate. Each patterned window was etched in KOH solution through the entire thickness of the Si wafer, leaving freestanding Si_3N_4 layers, upon which PLD BYZ films were deposited after the KOH etching while ALD BYZ films were fabricated before the etching. The supporting silicon nitride layer was removed by plasma-assisted chemical etching using SF_6 gas, leaving freestanding BYZ layers. For catalysis and current collection, 80 nm thick porous Pt layers were deposited using DC sputtering on both the cathode and anode sides.

Results and Discussion

A. Characterization of ALD BYZ Films. Growth rates of zirconia and yttria films were first investigated individually. The goal was to establish the temperature regime where films are deposited in a surface-controlled mode, i.e., in the ALD window. To find the optimal conditions for ALD of ZrO_2, we varied the deposition temperature

(20) Copel, M.; Gribelyuk, M.; Gusev, E. *Appl. Phys. Lett.* **2000**, *76*, 436–438.
(21) Perkins, C. M.; Triplett, B. B.; McIntyre, P. C.; Saraswat, K. C.; Haukka, S.; Tuominen, M. *Appl. Phys. Lett.* **2001**, *78*, 2357–2359.
(22) Kukli, K.; Forsgren, K.; Ritala, M.; Leskelä, M.; Aarik, J.; Hårsta, A. *J. Electrochem. Soc.* **2001**, *148*, F227–F232.
(23) Nakajima, A.; Kidera, T.; Ishii, H.; Yokoyama, S. *Appl. Phys. Lett.* **2002**, *81*, 2824–2826.
(24) Chang, J. P.; Lin, Y. S. *J. Appl. Phys.* **2001**, *90*, 2964–2969.
(25) Putkonen, M.; Niinistö, J. *J. Mater. Chem.* **2001**, *11*, 3141–3147.
(26) Putkonen, M.; Niinistö, J.; Kukli, K.; Sajavaara, T.; Karppinen, M.; Yamauchi, H.; Niinistö, L. *Chem. Vap. Deposition* **2003**, *9*, 207–212.
(27) Hausmann, D. M.; Kim, E.; Becker, J.; Gordon, R. G. *Chem. Mater.* **2002**, *14*, 4350–8.
(28) Putkonen, M.; Sajavaara, T.; Johansson, L. S.; Niinistö, L. *Chem. Vap. Deposition* **2001**, *7*, 44–50.
(29) de Rouffignac, P.; Park, J. S.; Gordon, R. G. *Chem. Mater.* **2005**, *17*, 4808–4814.
(30) Niinistö, J.; Putkonen, M.; Niinistö, L. *Chem. Mater.* **2004**, *16*, 2953–2958.
(31) Hatanpää, T.; Vehkamäki, M.; Mutikainen, I.; Kansikas, J.; Ritala, M.; Leskelä, M. *Dalton Trans.* **2004**, 1181–1188.

from 100 to 350 °C. In this experiment, the pulse time and the purging time were fixed at 0.5 and 30 s (10 sccm of Ar), respectively. We identified a plateau region at 150−250 °C, and the growth rate was 1.2 Å/cycle, which corresponds well to values reported in the literature.[27] The deposition rates at 100 and 300 °C were slightly higher at ∼1.4 Å/cycle. At 350 °C, the deposition rate was measured as ∼3.7 Å/cycle, and it was clear that this temperature was out of the ALD window. It was suspected that insufficient purging was responsible for the enhanced rate at the low deposition temperature (100 °C), which was also observed by others.[27] The Y_2O_3 growth rate was measured at 200−275 °C with a pulse time and purging time of 0.5 and 30 s (10 sccm of Ar), respectively. With the exception of the rate at 200 °C (∼0.5 Å/cycle), the films grew at a rate of ∼1.2 Å/cycle, which also matched the published value.[30] To measure the growth rate of BaO, we adjusted the cycles for ZrO_2 and BaO depositions with the cycle ratio Ba:Zr = 1:1, which stabilized BaO into the $BaZrO_3$ structure, which otherwise could form the undesired $BaCO_3$ blocking phase in the presence of CO_2 in ambient air. Since the common ALD window for ZrO_2 and Y_2O_3 is limited to around 250 °C, we varied the substrate temperature from 250 to 270 °C. As a result, the deposition rates fell in the range 1.1−1.2 Å/cycle normalized by the number of subcycles (one super cycle of BaO + ZrO_2 deposition consists of two subcycles: one Ba−O cycle and one Zr−O cycle) with a pulse time and purging time of 0.5 s (0.7 s for Ba pulses) and 30 s (10 sccm of Ar), respectively, which is close to the rate for ZrO_2. We also confirmed that the component films grew in the self-limited mode by measuring constant growth rates at varied pulsing times (0.5−2 s, 0.5−1 s for barium) with a fixed purging time (30 s of 10 sccm Ar), providing evidence that the process seems to be ALD, although there are several works showing a low thermal stability of our barium and zirconium precursors at our temperatures[27,31] (Figure 1). We found that at least 15 s of purging time should be applied to remove reaction products as well as the unreacted and adsorbed species completely. On the basis of this observation, we conclude that there is no interaction or chemical cross-talk between cycles preserving growth rate of individual oxides. Finally, we tried ALD of BaO + ZrO_2 + Y_2O_3 with the cycle ratio Ba:Zr:Y = 1:0.8:0.2 and a pulse time and purging time of 0.5 s (0.7 s for Ba pulses) and 30 s (10 sccm of Ar), respectively, and the resulting deposition rate was found to be ∼1.1 Å/cycle, which remained unchanged at 250−270 °C.

The XPS composition analysis confirmed that the targeted stoichiometry Ba:Zr:Y = 1:0.8:0.2 was successfully achieved by the corresponding ALD cycle ratio. The XPS depth profiling also showed that the composition remains similar throughout the entire film thickness, as shown in Figure 2. The XRD analysis on the as-deposited film, whose substrate temperature was 250 °C, indicated no crystal peak matching the $BaZrO_3$ diffraction spectra. However, when the samples were annealed at 600 °C in 250 Torr of oxygen for 2 h, the XRD spectra indicated the emergence of several characteristic $BaZrO_3$ peaks,

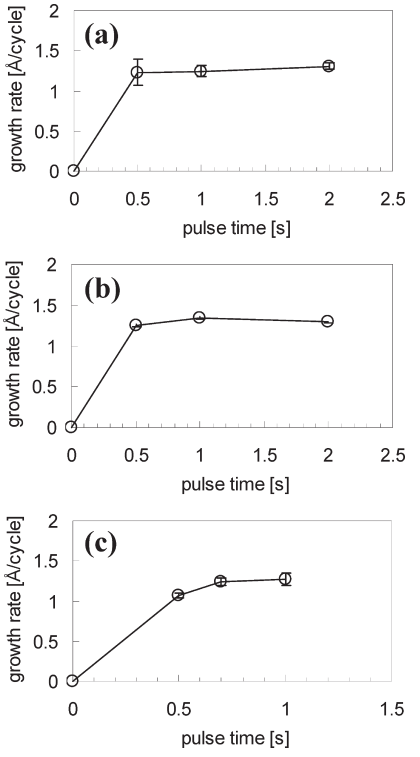

Figure 1. ALD growth rates of component oxides at 250 °C with a purging time of 30 s: (a) growth rate of zirconia with varied pulse times of 0.5−2 s; (b) growth rate of yttria with varied pulse times of 0.5−2 s; (c) growth rate of BaO + ZrO_2 films (one supercycle consists of two subcycles, one Ba−O cycle and one Zr−O cycle, and the growth rate is normalized by the number of subcycles) with varied pulse times of 0.5−1 s.

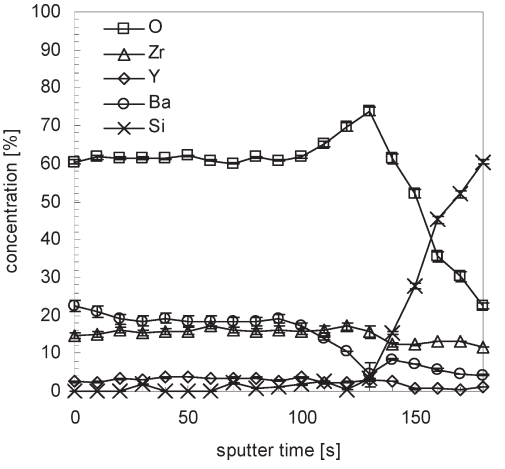

Figure 2. XPS depth profile of 20 nm thick ALD BYZ films deposited on Si(100) wafers with pulse ratios for Ba:Zr:Y = 1:0.8:0.2, where the deposition rate is approximately ∼1.3 Å/s.

indicating the evolution of the $BaZrO_3$ structure. The spectra also contained unknown peaks that were originally present in the spectra of the as-deposited ALD BYZ film. Additional annealing at 800 °C further crystallized the films into the $BaZrO_3$ habit, leaving only one unknown peak, which was not identified (Figure 3).

B. Fuel Cell Performance with PLD BYZ Membranes. In fuel cells with freestanding PLD BYZ electrolyte, the thickness of the BYZ layer was 130 nm, while each of the porous platinum electrodes on the anode and cathode side was 80 nm thick (Figure 4). We found that BYZ films

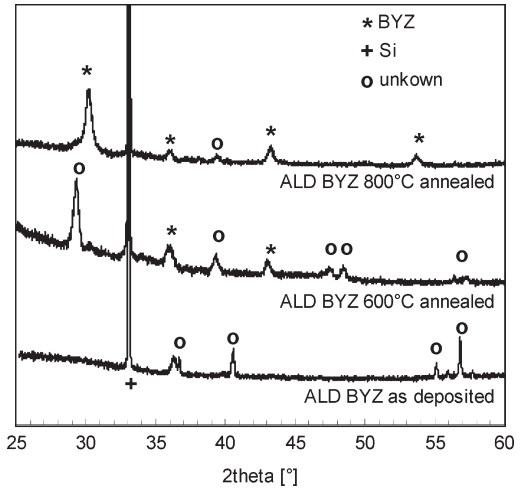

Figure 3. XRD of 110 nm thick ALD BYZ films on Si_3N_4-coated Si(100) substrates as deposited, postannealed at 600 °C, and postannealed at 800 °C for 2 h under 250 Torr of oxygen.

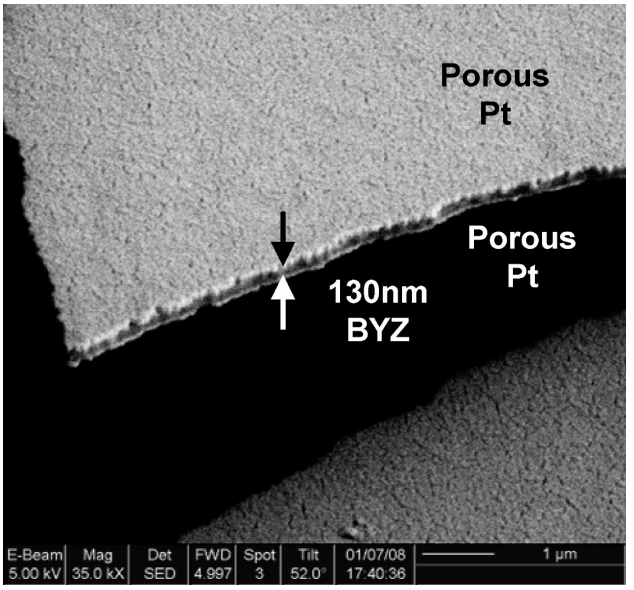

Figure 4. SEM image of freestanding PLD BYZ membrane-electrode assembly.

grown above 400 °C were too brittle to be freestanding BYZ membranes. In XRD analysis, it was observed that BYZ films further crystallized as the PLD temperature increased, and we suspect that grain formation during this increased crystallization (Figure 5) may be responsible for the mechanical failure of high-temperature PLD BYZ films. Therefore, we limited the PLD deposition temperature to 400 °C for fabrication of fuel cells. The performance of PLD BYZ membranes as fuel cell electrolytes was measured at temperatures from 300 to 450 °C (Figure 6). To acquire $I-V$ data, we started the voltage scan from open-circuit voltage (OCV) down to 0.1, 0.2, 0.2, and 0.45 V at 300, 350, 400, and 450 °C, respectively. Below these lower voltage limits, we observed that severe degradation occurred at the cathode and the morphology of the porous Pt electrode changed irreversibly (Figure 7). We speculate that an intense cathodic surface reaction at the electrode−electrolyte boundary with water

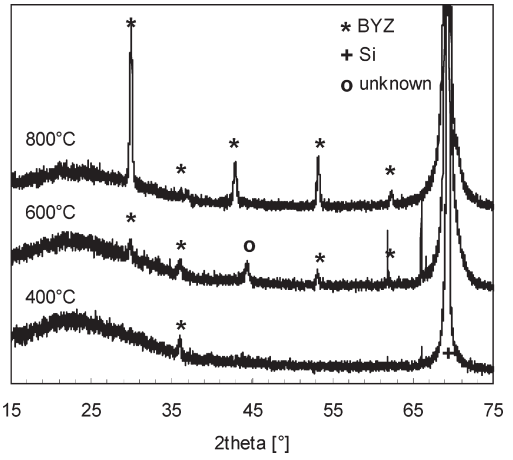

Figure 5. XRD patterns of 130 nm thick PLD BYZ films grown on Si_3N_4-coated Si(100) substrates at varied deposition temperatures (400−800 °C).

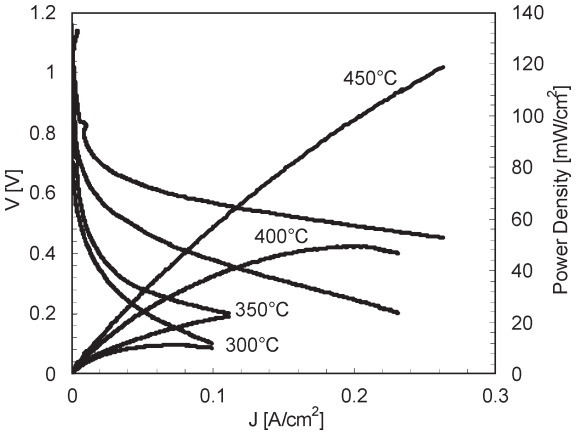

Figure 6. Polarization ($I-V$) curves and power density of PLD BYZ fuel cells measured at 300−450 °C.

generation may be responsible for the coarsening of the microstructure and, consequently, the loss of the triple phase boundary (TPB). A more in-depth investigation will be conducted to understand this degradation mechanism. The best-performing cells exhibited a maximum power density of 120 mW/cm^2 at 450 °C, 49 mW/cm^2 at 400 °C, 22 mW/cm^2 at 350 °C, and 11 mW/cm^2 at 300 °C (see Table 1). Cell OCVs measured above 300 °C in the range from 1.08 to 1.16 V were in general agreement with expected values, but OCVs measured at lower temperatures suggest the difficulty of achieving equilibrium (Table 1).

C. Fuel Cell Tests Employing ALD BYZ Membranes. A freestanding 110 nm thick BYZ film was prepared for the fuel cell test (Figure 8). The BYZ membrane was deposited at 250 °C, and it was not postannealed after deposition. We found that ALD BYZ postannealed was too brittle to be a freestanding film, as for PLD BYZ membranes deposited at 600−800 °C. The performance of the membrane as a fuel cell electrolyte was measured at temperatures from 200 to 400 °C (Figure 9). To avoid possible electrode degradation in the high-current region (or low-voltage region), we limited the minimum voltage to 0.2−0.4 V, depending on the measuring temperature.

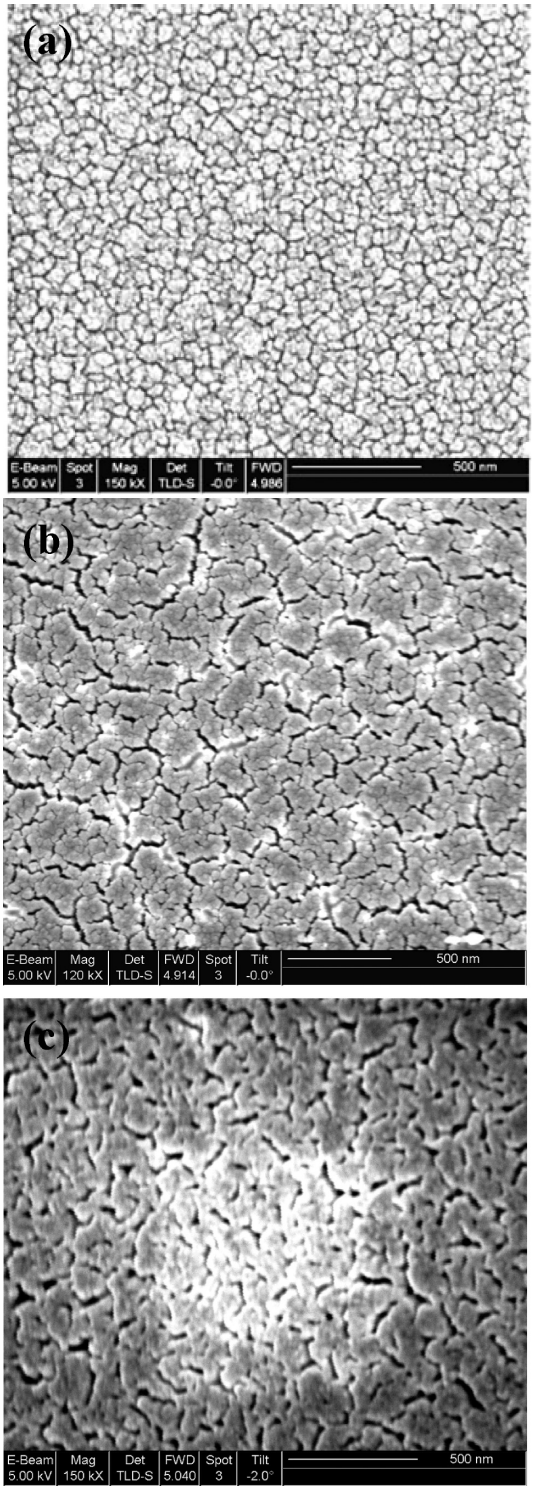

Figure 7. SEM image of porous Pt: (a) as deposited before fuel cell tests were made by the recipe developed by our group;[32] (b) on the cathode side of PLD BYZ after the fuel cell measurements at 450 °C; (c) on the cathode side of ALD BYZ after the fuel cell measurements at 400 °C.

Clearly, ALD BYZ cells exhibited better performance than those that employed PLD BYZ. In this case, the best-performing cells exhibited a maximum power density of 136 mW/cm^2 at 400 °C, 53 mW/cm^2 at 350 °C, 15 mW/cm^2 at 300 °C, 1.2 mW/cm^2 at 250 °C, and 0.1 mW/cm^2 at 200 °C (Table 1). The OCV values were measured in the range 1.08−1.10 V at 300−400 °C, while

Table 1. Comparison of OCV and Maximum Power Density of 130 nm Thick PLD BYZ Fuel Cells with 110 nm Thick ALD BYZ Fuel Cells at 200−450 °C

	PLD BYZ		ALD BYZ	
temp (°C)	OCV (V)	max power density (mW/cm^2)	OCV (V)	max power density (mW/cm^2)
200			0.83	0.1
250			0.97	1.2
300	1.15	11	1.08	15
350	1.16	22	1.10	53
400	1.14	49	1.09	136
450	1.12	120		

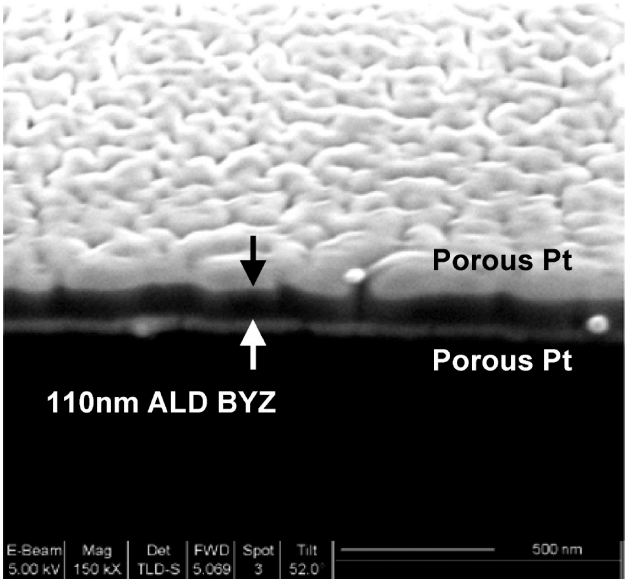

Figure 8. SEM image of freestanding ALD BYZ membrane-electrode assembly.

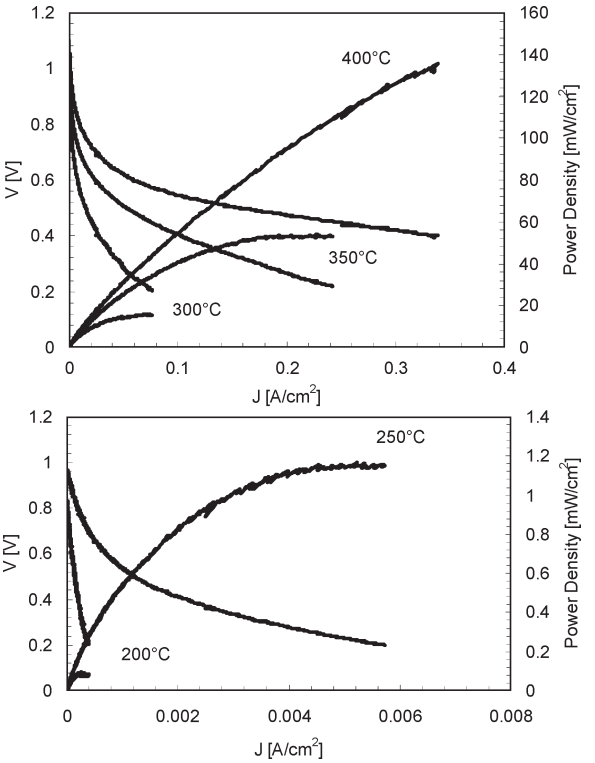

Figure 9. Polarization ($I-V$) curves and power density of ALD BYZ fuel cells measured at 200−400 °C.

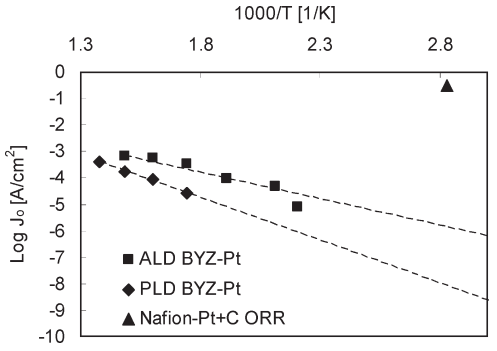

Figure 10. Arrhenius comparison of exchange current densities from PLD BYZ−Pt fuel cells, ALD BYZ fuel cells, and one data point referring to the Nafion−Pt system with hydrogen−air.[33]

low OCV around 0.8−0.9 V was observed at 200−250 °C, possibly due to poor equilibration with the gas phase at these temperatures (Table 1). In comparison with the PLD BYZ performance, we found that the power density was enhanced up to a factor of 2−3.

D. Performance Evaluation of PLD BYZ and ALD BYZ Membranes. To our knowledge, the power densities depicted in Figures 6 and 9 and in Table 1 indicate the highest densities reported to date at the lowest operating temperatures for a PCFC employing a BYZ electrolyte membrane. Interestingly, 136 mW/cm^2 was achieved at 400 °C in a PCFC employing BYZ fabricated by ALD, while 120 mW/cm^2 was achieved at 450 °C in a PCFC employing BYZ fabricated by PLD. This trend was also observed in the case of exchange current densities.

In this regard, the $I-V$ curves were evaluated through numerical fitting to a standard Tafel polarization model. We confirmed that our nanoscale BYZ films conduct protons after exposure to humidified environments, and the ionic conductivity is close to the reference bulk values in the absence of significant grain separation in a previous work.[33] Excluding the ohmic loss across the membrane consisting of a few grains, the resulting fuel cell output voltage associated with drawing current can be described as

$$V_{\text{cell}} = V_{\text{OCV}} - \eta_{\text{electrodes}} \tag{2}$$

where V_{OCV} is the open circuit voltage and $\eta_{\text{electrodes}}$ is the sum of the respective overpotentials at the electrodes. At currents higher than the exchange current density (j_0), which characterizes the relative forward and reverse electrode reaction rate at equilibrium, the dependence of the electrode overpotential on current can be represented by the following Tafel equation, which describes the activation losses:

$$\eta_{\text{electrodes}} = \frac{RT}{\alpha nF} \ln \frac{j}{j_0} \tag{3}$$

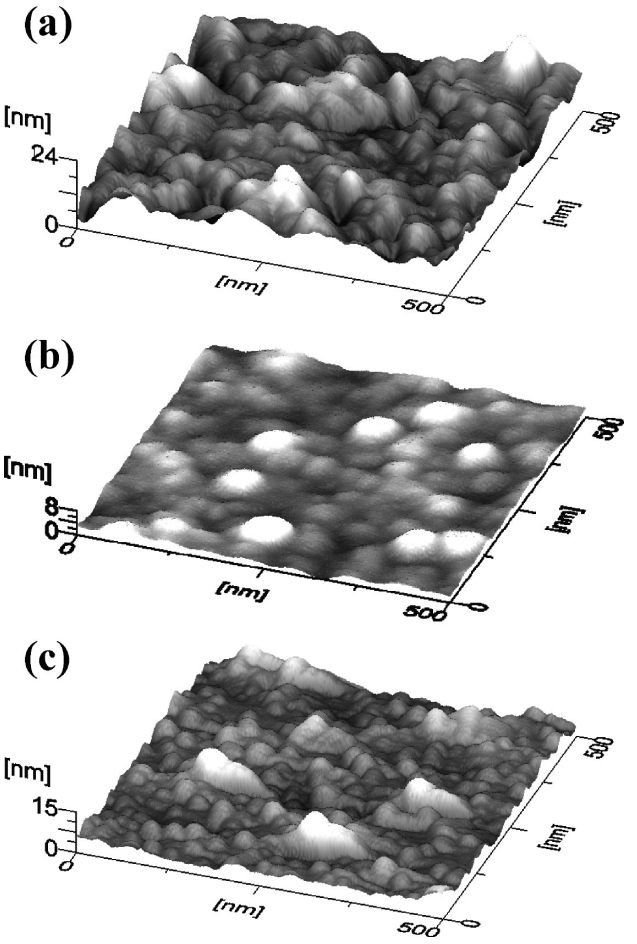

Figure 11. Surface morphology: (a) 130 nm thick PLD BYZ film deposited at 400 °C; (b) 110 nm thick ALD BYZ film as deposited; (c) ALD BYZ film postannealed at 600 °C measured by AFM. All of the films were grown on Si_3N_4-coated Si(100) wafers.

where α is the charge transfer coefficient, j is the generated current density, R is the universal gas constant, T is the temperature, and F is Faraday's constant. The charge transfer coefficient and the exchange current density are determined by extrapolating plots of log j versus $\eta_{\text{electrodes}}$ to $\eta_{\text{electrodes}} = 0$. High j_0 values indicate not only that the rate of reaction at equilibrium is fast but also that the number of possible reaction sites is large.[34] Fitting results suggest that the electrode losses, which were assumed to be dominated by cathodic reactions,[35] account for most of the energy losses in the fuel cell operation, and the ohmic loss due to ion transport across the PLD BYZ electrolyte was negligibly small. The charge transfer coefficient calculated from the model was in the range 0.2−0.3, in good agreement with the reference values for cathode reactions in typical proton conducting fuel cells (∼0.25).[36] In the analysis of j_0, ALD BYZ exhibited significantly higher exchange current densities compared to PLD BYZ by 3−10 times, with a smaller activation energy in the Arrhenius relation (Figure 10).

(32) Wang, X.; Huang, H.; Holme, T.; Tian, X.; Prinz, F. B. *J. Power Sources* **2008**, *175*, 75–81.
(33) Shim, J. H.; Gür, T. M.; Prinz, F. B. *Appl. Phys. Lett.* **2008**, *92*, 253115.
(34) O'Hayre, R.; Cha, S.; Colella, W.; Prinz, F. B. Fuel Cell Fundamentals; Wiley: New York, 2006.
(35) Hibino, T.; Hashimoto, A.; Suzuki, M.; Sano, M. *J. Electrochem. Soc.* **2002**, *149*, A1503–A1508.
(36) Wang, Z. H.; Wang, C. Y.; Chen, K. S. *J. Power Sources* **2001**, *94*, 40–50.

We speculate that the difference in the surface morphology of PLD and ALD films may be responsible for this enhancement. In the AFM analysis, we observed that the ALD films showed close-packed circular grains with surface roughness (root mean square, rms) of 0.97 nm and a surface topology variation of less than 8 nm from the lowest point to the peak point on an area of 500 nm × 500 nm, while the PLD films consisted of loosely packed grains with a larger roughness of 2.0 nm and a topological range of 20 nm from the lowest point to the highest point on the same area (Figure 11).

Crystallization seems to greatly affect surface morphology. As supporting evidence, it was observed that the surface of ALD BYZ became roughened with increasing surface roughness from 0.97 nm rms to 2.0 nm as the film was crystallized by the 600 °C postannealing (Figure 11). Smoother surfaces with grains closely interconnected in the ALD BYZ films are likely to provide more surface reaction sites with the sputtered platinum layer than the rougher PLD BYZ films. Accordingly, it is suspected that the smoother ALD BYZ electrolyte/electrode interface may be responsible for increased exchange current density.

Another possibility is the interplay between surface energy and polymorphism. When the bulk Gibbs free energy of formation of one phase versus the other is large, the material adopts the phase with the more negative Gibbs energy. This consideration becomes especially important and relevant as the grain size and film thickness approach the nanoscale regime. Indeed, low-temperature synthesis methods in many cases yield amorphous oxide films (e.g., for Si, Nb, Al, Ta). A thermodynamic study for oxide films on single-crystal Al indicated that, below a critical thickness, the equilibrium oxide film is amorphous.[37] Similarly, Navrosky and co-workers have demonstrated that, below about 10 nm grain size, amorphous zirconia is more stable than its crystalline forms of monoclinic and tetragonal zirconia.[38,39] More interestingly, they reported significantly lower surface energy for amorphous zirconia (0.5 J/m^2) compared to monoclinic (6.4 J/m^2) and tetragonal forms (2.1 J/m^2).[40] The relative resistance to corrosion exhibited by many glassy metal alloys in comparison to that of their crystalline structures is also known, exemplified by the relatively higher chemical stability of the amorphous phase under specific conditions.

Assuming this trend holds also for BYZ, then it is likely that the amorphous structure of the ALD BYZ membrane used in this study may have a lower surface energy than its cubic counterpart. The low surface energy surface of BYZ would allow better wetting for the Pt layer, whose surface energy is much higher (2.7 J/m^2), hence providing a higher density of interfacial reaction sites (i.e., triple phase boundary) between the BYZ membrane and the porous Pt electrode that results in higher cell performance and exchange current density. Although the surface energy for cubic BYZ has not been reported in the literature, the energy of the $BaZrO_3$ (001) surface with BaO (001) termination was calculated from first principles to be 1.064 J/m^2, while for the ZrO_2 (001) terminated surface it is 1.032 J/m^2.[41] Again, the lower surface energy assumption, if true, would provide an advantage for the amorphous ALD BYZ membrane over the crystalline PLD BYZ membrane in terms of performance. However, the validity of this assumption requires further study and verification.

Conclusion

We have successfully fabricated ultrathin BYZ membranes as electrolytes of fuel cells using PLD and ALD techniques. Fuel cells with 130 nm thick PLD BYZ electrolyte were successfully fabricated and tested. The maximum power density of PLD BYZ fuel cells was measured as 11−120 mW/cm^2 at 300−450 °C. ALD BYZ was synthesized with the target composition of Ba:Zr:Y = 1:0.8:0.2. In comparison to PLD BYZ, the 110 nm thick ALD BYZ electrolyte demonstrated improved fuel cell performance, showing up to 136 mW/cm^2 at 200−400 °C as the maximum power density. This may be attributed to higher electrochemical reaction site densities in ALD BYZ films, resulting in higher exchange current densities. Further investigation is needed for a quantitative understanding of the difference in behavior between fuel cells containing ALD and PLD BYZ electrolyte membranes.

Acknowledgment. Financial support from the ONR (Grant No. 1031010-2-TDAGP) and ONR-MURI (Grant No. 1111078-1-SXCAP) programs are gratefully acknowledged. We also acknowledge the Fuel Cell Consortium Project and Global Climate and Energy Project (GCEP) at Stanford University for partial support.

(37) Jeurgens, L. P. H.; Sloof, W. G.; Tichelaar, F. D.; Mittemeijer, E. J. *Phys. Rev. B* **2000**, *62*, 4707–4719.
(38) Navrostky, A. *J. Mater. Chem.* **2005**, *15*, 1883–1890.
(39) Molodetsky, I.; Navrostky, A.; Paskowitz, M. J.; Leppert, V. J.; Risbud, S. H. *J. Non-Cryst. Solids* **2000**, *262*, 106–113.
(40) Pitcher, M. W.; Ushakov, S. V.; Navrostky, A.; Woodfield, B. F.; Li, G.; Boerio-Goates, J.; Tissue, B. M. *J. Am. Ceram. Soc.* **2005**, *88*, 160–167.
(41) Merinov, B.; van Duin, A.; Haile, S. M.; Goddard, W. A., III. Reactive Force Fields for Y-doped $BaZrO_3$ Electrolyte and Ni-anode. Potential Cathode Materials for Application in Protonic Ceramic Fuel Cells; DOE Report, OSTI ID: 836617, **2004**.